

## THE HARD TO SOFT TRANSITION OF GX 339–4 AS SEEN BY *INSIGHT*–HXMT

HONGHUI LIU<sup>1</sup>, COSIMO BAMBI<sup>1,†</sup>, JIACHEN JIANG<sup>2</sup>, JAVIER A. GARCÍA<sup>3,4</sup>, LONG JI<sup>5</sup>, LINGDA KONG<sup>6</sup>, XIAOQIN REN<sup>7,8</sup>, SHU ZHANG<sup>7,8</sup>, SHUANGNAN ZHANG<sup>7,8</sup>

*Draft version June 7, 2023*

### ABSTRACT

We present an analysis of the relativistic reflection spectra of GX 339–4 during the hard-to-soft transition of its 2021 outburst observed by *Insight*–HXMT. The strong relativistic reflection signatures in the data suggest a high black hole spin ( $a_* > 0.86$ ) and an intermediate disk inclination angle ( $i \approx 35^\circ$ – $43^\circ$ ) of the system. The transition is accompanied by an increasing temperature of the disk and a softening of the corona emission while the inner disk radius remains stable. Assuming a lamppost geometry, the corona height is also found to stay close to the black hole across the state transition. If we include the Comptonization of the reflection spectrum, the scattering fraction parameter is found to decrease during the state transition. We also perform an analysis with a reflection model designed for hot accretion disks of stellar mass black holes where the surface of the innermost accretion disk is illuminated by emission from the corona and the thermal disk below. Our results support the scenario in which the state transition is associated with variations in the corona properties.

*Subject headings:* accretion, accretion disks — black hole physics — X-rays: binaries

### 1. INTRODUCTION

The outbursts of black hole X-ray binaries (XRBs) are characterized by orders of magnitude change in the X-ray luminosity (Remillard & McClintock 2006). It is generally believed that there are dramatic changes in the geometry of the accretion flow during the outburst (e.g. Zdziarski & Gierliński 2004; Done et al. 2007; Plant et al. 2015). If plotting on the hardness intensity diagram (HID), the outburst often moves anticlockwise to form a q-shaped pattern (e.g. Fender et al. 2004; Belloni et al. 2005). At the early stage of the outburst, the source luminosity is low and its X-ray spectrum is usually dominated by a hard power-law component, which is thought to be originated from inverse Compton scattering of seed photons by a hot ( $\sim 100$  keV) corona (e.g. Dove et al. 1997; Zdziarski & Gierliński 2004). This is the so called low hard (LH) state that is located at the

lower right corner of the HID. At this phase, the source spectrum remains hard as it gets brighter. Moreover, a high-energy cut-off of the broadband X-ray spectrum is commonly observed and is thought to be determined by the coronal temperature. The energy of this cut-off is found to decrease with the source luminosity (e.g. Yamaoka et al. 2005; Miyakawa et al. 2008; Joinet et al. 2008, but see Yan et al. 2020 for a opposite correlation at even lower luminosities).

At some point, the source makes a fast transition from the hard state to a thermal-emission-dominated soft state through the intermediate states (e.g. Homan & Belloni 2005; Belloni 2010). The transition, which can happen in a wide range of luminosities, often completes in a few days and is associated with softening of the source spectrum. This softening is a result of the increasing contribution from the disk thermal emission and steepening of the corona emission. Overall, the X-ray spectrum appears as pivoting around certain energy (e.g. Del Santo et al. 2008). The cut-off energy tends to rise during the hard to soft transition (e.g. Motta et al. 2009) and in some cases, no high-energy cut-off is found up to  $\sim 1$  MeV in the soft state (e.g. Tomsick et al. 1999; Belloni et al. 2006).

A commonly accepted scenario to explain the state transition is the truncated disk model (e.g. Esin et al. 1997). In this scenario, the standard geometrically thin and optically thick accretion disk (Shakura & Sunyaev 1973) is truncated at large radius in the low hard state when the accretion rate is low. A hot radiatively inefficient accretion flow is filled between the truncation radius and the black hole (e.g. Narayan 2005). As the accretion rate increases, the disk moves closer to the black hole, which produces stronger disk thermal emission. X-ray observations of XRBs have provided good evidence that

<sup>1</sup> Center for Field Theory and Particle Physics and Department of Physics, Fudan University, 200438 Shanghai, China. †E-mail: bambi@fudan.edu.cn

<sup>2</sup> Institute of Astronomy, University of Cambridge, Madingley Road, Cambridge CB3 0HA, UK

<sup>3</sup> Cahill Center for Astronomy and Astrophysics, California Institute of Technology, 1216 E. California Boulevard, Pasadena, CA 91125, USA

<sup>4</sup> Dr. Karl Remeis-Observatory and Erlangen Centre for Astroparticle Physics, Sternwartstr. 7, D-96049 Bamberg, Germany

<sup>5</sup> School of Physics and Astronomy, Sun Yat-Sen University, 519082 Zhuhai, China

<sup>6</sup> Institut für Astronomie und Astrophysik, Kepler Center for Astro and Particle Physics, Eberhard Karls, Universität, Sand 1, D-72076 Tübingen, Germany

<sup>7</sup> Key Laboratory for Particle Astrophysics, Institute of High Energy Physics, Chinese Academy of Sciences, 100049 Beijing, China

<sup>8</sup> University of Chinese Academy of Sciences, Chinese Academy of Sciences, 100049 Beijing, China

the disk is truncated at large radius in low luminosities (e.g. Tomsick et al. 2009) and reaches the innermost stable circular orbit (ISCO) in the high flux soft state (e.g. Gierliński & Done 2004; Steiner et al. 2010). However, it remains to be known at which point the disk exactly reaches the ISCO and what mechanism triggers the state transition. Moreover, in some cases, the measurements of the size of inner edge are found to be controversial and model dependent (e.g. Dzielak et al. 2019; Mahmoud et al. 2019; Zdziarski et al. 2021).

Relativistic reflection component, namely the reflected corona emission by the optically thick accretion disk extending close to the black hole, is a powerful tool to probe the spacetime properties (e.g. Reynolds 2014; Bambi 2017; Liu et al. 2019; Bambi et al. 2021) and the geometry of the accreting system (e.g. García et al. 2015; Wilkins & Gallo 2015; Wang et al. 2020; Szanecki et al. 2020). One of the main features of the relativistic reflection component is the broad iron line around 6.4 keV. The broad line profile is a result of skewed iron K lines due to the strong relativistic effect near the black hole (e.g. Doppler effect, light bending and gravitational redshift, Fabian et al. 2000; Dauser et al. 2010). This is why this broad line feature can be used to map the innermost regions around the accreting black hole (e.g. Fabian et al. 1989).

GX 339–4 is a classical low mass X-ray binary located at 8–12 kpc with a black hole mass of 4–11  $M_{\odot}$  (Zdziarski et al. 2019). Strong relativistic reflection signatures have been found in this source in the hard and soft states (e.g. García et al. 2015; Miller et al. 2004; Liu et al. 2022). Previous studies have found that the black hole in GX 339–4 has a very high spin ( $a_{*} \sim 0.95$ , García et al. 2015; Parker et al. 2016). The inclination angle of the accretion disk should have an intermediate value (Fürst et al. 2015; Parker et al. 2016). The source goes into bright outburst every a few years and thus is an ideal object for the study of the accretion flow through different spectra states. Recently, the hard-to-soft transition of GX 339–4 has been studied by Sridhar et al. (2020) with *RXTE*/PCA data based on reflection analysis. The inner edge of the accretion disk was found to be close to ISCO during the transition. Starting from February 2021, GX 339–4 went into a new outburst that lasted for a few months. The hard to soft transition of this outburst has been captured by the Chinese X-ray satellite Hard X-ray Modulation Telescope (dubbed *Insight*–HXMT, Zhang et al. 2014). Therefore, we study the *Insight*–HXMT data to understand the evolution of the accretion geometry.

In this paper, we aim at studying the relativistic reflection spectra of GX 339–4 during its 2021 outburst with *Insight*–HXMT data. In Sec. 2, we describe the data reduction process. The spectral fitting results are presented in Sec. 3. We discuss the results in Sec. 4.

## 2. OBSERVATION AND DATA REDUCTION

*Insight*–HXMT monitored the 2021 outburst of GX 339–4 with observations on nearly every day (see Fig. 1). Starting from 2021 March 25, the source made a fast transition from the hard state to the soft state in about one week. The soft to hard transition, which should happen at a lower luminosity, was not captured because of the high background of *Insight*–HXMT. The

purpose of this work is to study the evolution of the system during the state transition. Therefore, we select *Insight*–HXMT observation data during the transition and investigate their broadband energy spectra. Details about the selected *Insight*–HXMT observations are listed in the appendix.

The low-energy (LE), medium-energy (ME) and high-energy (HE) detectors onboard *Insight*–HXMT cover the energy range of 1–250 keV (Chen et al. 2020; Cao et al. 2020; Liu et al. 2020; Zhang et al. 2020). The energy spectra are extracted following the HXMT Data Reduction Guide v2.04<sup>9</sup> and using the software HXMTDAS v2.04. The background spectra are estimated using the scripts `hebkmap`, `mebkmap` and `lebkmap` (Liao et al. 2020a; Guo et al. 2020; Liao et al. 2020b). As indicated in Tab. 2, short exposures on the same day are merged to increase the signal to noise ratio. Before merging the data, we first check the lightcurve and hardness ratio and confirm that there are no significant flares or dips. In the end, we obtain energy spectra for seven epochs. The spectra are then binned to ensure a minimal signal to noise ratio of 25 before fitting them to physical models. We use data in 2–10 keV, 10–25 keV and 30–100 keV bands for LE, ME and HE respectively.

## 3. SPECTRAL ANALYSIS

Spectral fittings are conducted with XSPEC v12.11.1 (Arnaud 1996). We implement element abundances of Wilms et al. (2000) and cross-sections of Verner et al. (1996).  $\chi^2$  statistics are used to find the best-fit values and uncertainties (at 90% confidence level unless otherwise specified) of the model parameters.

### 3.1. Relativistic reflection features

As the first step, we fit the seven spectra simultaneously with a simple absorbed continuum model which consists of a multicolor disk component (`diskbb`; Mitsuda et al. 1984), a power-law component with a high energy cutoff (`cutoffpl`) and a Galactic absorption model (`tbabs`; Wilms et al. 2000). In XSPEC notation, the model can be written as `constant*tbabs*(diskbb + cutoffpl)`. The `constant` is required to quantify the cross-normalization between the three instruments onboard *Insight*–HXMT. The column density ( $N_{\text{H}}$ ) of the `tbabs` is set as a free parameter and tied across all spectra.

The ratios between the data and the best-fit models for the seven spectra are shown in Fig. 2, from which we can identify the missing model components. We can see that the common features in Fig. 2 are a broad excess around 6–7 keV and a hump around 30 keV. These features are commonly seen in the X-ray spectra of black hole XRBs (e.g. Miller et al. 2013; García et al. 2015; Jiang et al. 2019a) and can be explained by the corona emission being reflected by the optically thick accretion disk (e.g. Ross et al. 1999). The position of the neutral iron  $K\alpha$  fluorescent line (6.4 keV) is marked with vertical dashed line in Fig. 2. The broad emission profile around this line is a result of relativistically skewed iron

<sup>9</sup> The guide can be found from here: <http://hxmtweb.ihep.ac.cn/SoftDoc/496.jhtml>. We follow the extraction approach provided here: <https://code.ihep.ac.cn/jldirac/insight-hxmt-code-collection/-/tree/master/version2.04>.

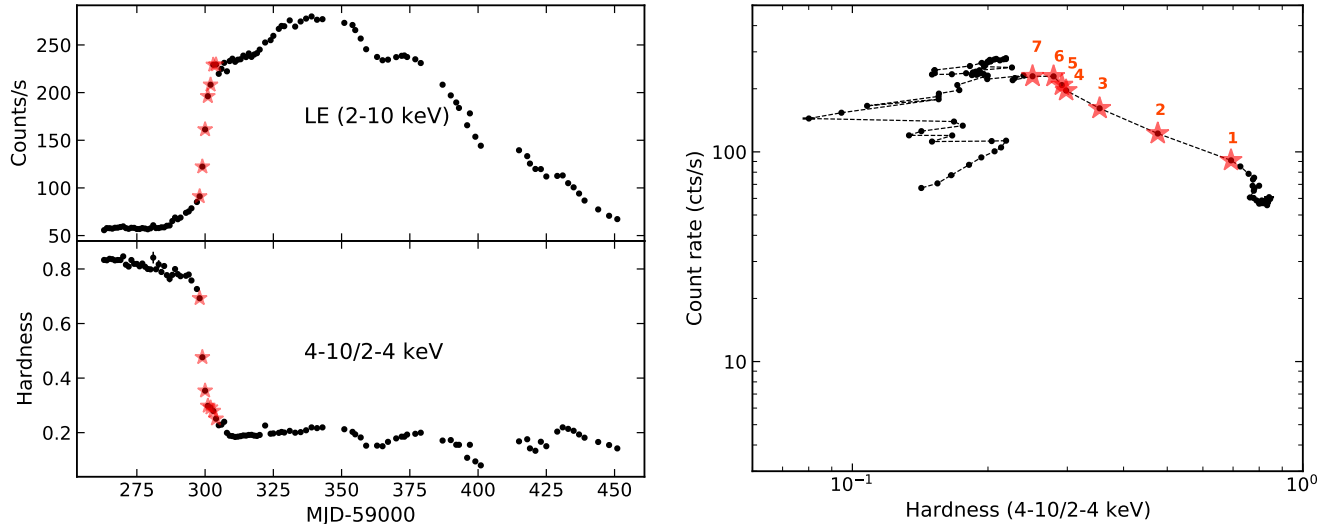


FIG. 1.— (left): The observation log of GX 339–4 from *Insight*–HXMT Low Energy (LE) instruments. The hardness is defined as the ratio between count rates in 4–10 keV and 2–4 keV. (right): The hardness intensity diagram of GX 339–4 from *Insight*–HXMT. Each point represents data from one day and is marked with the epoch number. The red color denotes the observations analyzed in this work.

K lines. Moreover, the electron down scattering of high energy photons and photoelectric absorption on the disk leads to the “Compton hump” around 30 keV (George & Fabian 1991).

### 3.2. Spectral fitting with reflection models

To model the relativistic reflection features, we implement the widely used reflection model `relxill` v1.4.3 (García et al. 2014). The full model reads as `constant*tbabs*(diskbb+relxill+cutoffpl)` (Model 1). With this model, we are able to measure parameters of the system like the black hole spin ( $a_*$ ), the inclination angle ( $i$ ) of the accretion disk with respect to our line of sight and the size of the disk inner edge ( $R_{\text{in}}$ ). The seven spectra are fitted simultaneously. The column density of the Galactic absorption ( $N_{\text{H}}$ ), the black hole spin, the inclination angle and the iron abundance of the system should not change on the short timescale we are seeing. Therefore, these parameters are linked across all spectra during the spectral fitting. The reflection fraction parameter of `relxill` is set to  $-1$  so that the model returns only the reflection component. The outer radius of the disk  $R_{\text{out}}$  is fixed at  $400 R_{\text{g}}$  (where  $R_{\text{g}} = GM/c^2$  is the gravitational radius,  $M$  is the black hole mass).

#### 3.2.1. Lamppost geometry

The emissivity profile, defined as the radial dependence of the intensity of reflected emission, is a vital component of the reflection model. In principle, if the corona geometry is known, the emissivity profile can be self-consistently calculated. Therefore, we implement the `relxillp` (Model 1A), which is one of the models in the `relxill` package. The model assumes a lamppost geometry (Dauser et al. 2013), in which the corona is a point source above the black hole at certain height ( $h$ ). This model offers a good fit with  $\chi^2/\text{d.o.f.}=3697.6/3384$ . The best-fit values are shown in Tab. 1. The spectral components and residuals of the best-fit model are shown in Fig 3, from which we do not see significant unresolved features. With this model, we can fit with both the spin

parameter and the inner disk radius free. There is usually strong degeneracy between the two parameters (e.g. Dauser et al. 2013). Our data can break this degeneracy because the disk extends very close to the ISCO (Fabian et al. 2014). If we fix the spin parameter at the maximum value the model allows ( $a_* = 0.998$ ),  $R_{\text{in}}$  is still not constrained for Epoch 1 but is smaller than twice of the ISCO from Epoch 4 to Epoch 7 ( $\chi^2/\text{d.o.f.}=3697.6/3385$ ). Moreover, if we set  $R_{\text{in}}$  at ISCO for all epochs, the spin is measured to be  $0.93 \pm 0.01$  ( $\chi^2/\text{d.o.f.}=3704.0/3391$ ).

#### 3.2.2. Broken power-law emissivity

The other method commonly used to deal with the emissivity profile is to fit it phenomenologically with a broken power-law (i.e.,  $\epsilon \propto 1/r^{q_{\text{in}}}$  for  $R_{\text{in}} < r < R_{\text{br}}$  and  $\epsilon \propto 1/r^{q_{\text{out}}}$  for  $R_{\text{br}} < r < R_{\text{out}}$  where  $R_{\text{br}}$  is the breaking radius). We test both the power-law emissivity ( $q_{\text{in}} = q_{\text{out}}$ ) and the broken power-law emissivity (implemented with the model `relxill`) to look for a better description of the data. In the latter case, we fix the outer index fixed at 3 ( $q_{\text{out}} = 3$ ), which is the value predicted by Newtonian limit for a compact corona. Moreover, for the first three epochs, the inner index ( $q_{\text{in}}$ ) and the breaking radius ( $R_{\text{br}}$ ) can not be constrained by the data. Therefore, we fix  $q_{\text{in}}$  at 3 for those data. The broken power-law emissivity provides a better statistics ( $\chi^2/\nu = 3673.1/3383$ ), with the  $\chi^2$  lowered by 13 with 2 more free parameters. The best-fit values for the broken power-law emissivity (Model 1B) are shown in Tab. 3.

#### 3.2.3. High-density reflection

The disk density ( $n_e$ ) of the models above is fixed at  $10^{15} \text{ cm}^{-3}$ . This value might be appropriate for massive black holes but XRBs with a stellar mass black hole are known to have a higher density (e.g. Jiang et al. 2019a,b). Therefore, we implement the `relxillD` model (assuming a broken power-law emissivity, Model 1C) in which  $\log(n_e)$  is allowed to vary between 15 and 19 (García et al. 2016). The best-fit parameters are shown in Tab. 4. Compared to the model above, the high-density model

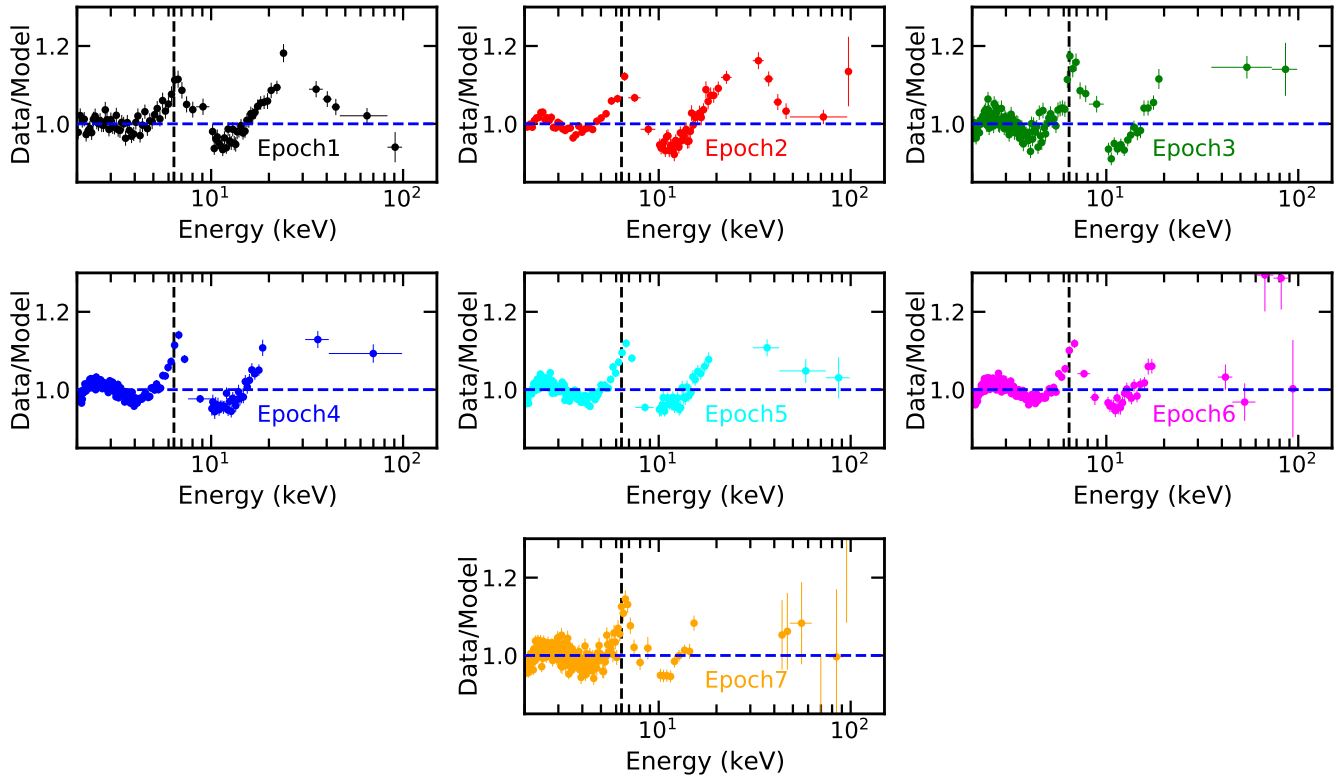


FIG. 2.— Data to model ratios for an absorbed continuum model `tbabs*(diskbb+cutoffpl)` for the seven epochs. The vertical line marks the position of 6.4 keV. Data are rebinned for visual clarity.

slightly improves the  $\chi^2$  by 9 with 7 more degrees of freedom and provides consistent constraints on the spin parameter and the inclination angle. Five out of the seven observations require a higher density than  $10^{15} \text{ cm}^{-3}$ . The measurements on the ionization parameter are systematically lowered. This is expected since a higher density leads to stronger soft X-ray emission, which is similar to the effect of a higher ionization parameter.

### 3.2.4. The Comptonized continuum

The models tested above provide good fits to the data. However, the column density of the `tbabs` component is higher than what reported in previous spectral analysis (e.g.  $7.7 \pm 0.2 \times 10^{21} \text{ cm}^{-2}$  in Parker et al. 2016, with the same versions of abundances and cross-sections). This is recovered if we replace `cutoffpl` with a physically motivated Comptonization model `nthcomp` (Zdziarski et al. 1996; Życki et al. 1999). The reflection component is also changed to the corresponding flavor `relxillcp` (Model 2). We link the seed photon temperature for the `nthcomp` model to the  $T_{\text{in}}$  parameter in `diskbb`. The best-fit parameters for this model are shown in Tab. 5. Compared with `relxill`, this model increases the statistics by  $\Delta\chi^2 = 64$  but lowers the column density of the Galactic absorption to  $7.3 \pm 0.6 \times 10^{21} \text{ cm}^{-2}$ . This is because the Comptonization model considers cutoffs at both low and high energy ends. Therefore, the X-ray luminosity estimated from the Comptonization model should be more realistic than that from the model with `cutoffpl`. We also note that our data cannot well constrain the coronal temperature (or the high energy cutoff).

### 3.2.5. Distant reflector

The spectra of GX 339–4 may require a distant reflection component to fit a possible narrow-line feature (e.g. Wang-Ji et al. 2018; Sridhar et al. 2020). To test this possibility, we add a `xillver` (García & Kallman 2010; García et al. 2013) component to Model 1A. The relativistic reflection model assumes a broken power-law emissivity profile. The ionization parameter of this distance reflection component is fixed at  $\log(\xi) = 0$ . The other parameters of the distance reflector are linked to the corresponding values in the relativistic reflection component. Adding this component improves the  $\chi^2$  by only 10 with 7 more free parameters.

To test if our data quality is good enough to distinguish such a distant reflector, we simulate 1000 spectra with a model that includes a distant reflection component. The response files, exposure time and model parameters (Tab. 1) are taken from our Epoch 5 which has the longest exposure. The flux (0.1–100 keV) of the distant reflection component is set to be 2% (e.g. Sridhar et al. 2020) of the relativistic component. Then we fit the spectra with two models: one without the distant reflection and the other includes it. The latter model always gives a better statistics with  $\Delta\chi^2 > 50$  and one more degrees of freedom, which indicates that the distant component can be detected if it exists. Therefore, we conclude that, for the observation with the longest exposure time, the distant reflection component can be detected if its flux is larger than 2% of the relativistic component. The reason why we do not detect the distant component in our analysis could be that its flux is lower than the limit provided by our data quality. Sim-



TABLE 1  
BEST-FIT VALUES WITH THE LAMPPPOST GEOMETRY (MODEL 1A).

Component	Parameter	Epoch 1	Epoch 2	Epoch 3	Epoch 4	Epoch 5	Epoch 6	Epoch 7
<b>tbabs</b>	$N_{\text{H}}$ ( $10^{22}$ cm $^{-2}$ )				$0.99^{+0.04}_{-0.06}$			
<b>diskbb</b>	$T_{\text{in}}$ (keV)	$0.50^{+0.03}_{-0.03}$	$0.548^{+0.014}_{-0.01}$	$0.656^{+0.008}_{-0.008}$	$0.725^{+0.011}_{-0.008}$	$0.725^{+0.01}_{-0.009}$	$0.766^{+0.006}_{-0.007}$	$0.757^{+0.011}_{-0.007}$
<b>relxillp</b>	$a_*$				$> 0.95$			
	$h$ ( $R_{\text{g}}$ )	$3.5^{+P}_{-P}$	$3.1^{+0.5}_{-0.5}$	$2.0^{+4}_{-P}$	$2.20^{+0.21}_{-0.1}$	$2.06^{+0.18}_{-P}$	$2.35^{+0.28}_{-0.29}$	$2.03^{+0.24}_{-P}$
	Incl				$42.0^{+1.3}_{-1.4}$			
	$A_{\text{Fe}}$ (solar)				$10.0^{+P}_{-0.6}$			
	$R_{\text{in}}$ (ISCO)	$70^{+P}_{-P}$	$1.4^{+0.7}_{-P}$	$3.2^{+1.2}_{-1.9}$	$1.56^{+0.08}_{-0.07}$	$1.44^{+0.08}_{-0.09}$	$1.62^{+0.12}_{-0.13}$	$1.6^{+0.1}_{-0.1}$
	$\log(\xi)$	$4.29^{+0.06}_{-0.06}$	$3.89^{+0.17}_{-0.23}$	$4.51^{+0.06}_{-0.11}$	$3.71^{+0.09}_{-0.08}$	$4.06^{+0.22}_{-0.2}$	$4.14^{+0.2}_{-0.19}$	$3.79^{+0.13}_{-0.12}$
<b>cutoffpl</b>	$\Gamma$	$1.696^{+0.018}_{-0.013}$	$2.087^{+0.028}_{-0.019}$	$2.260^{+0.06}_{-0.019}$	$2.460^{+0.021}_{-0.03}$	$2.451^{+0.024}_{-0.019}$	$2.511^{+0.028}_{-0.024}$	$2.55^{+0.1}_{-0.08}$
	$E_{\text{cut}}$ (keV)	$150^{+20}_{-20}$	$160^{+40}_{-20}$	$> 400$	$> 400$	$> 330$	$> 410$	$130^{+50}_{-60}$
<b>cflux</b>	( $10^{-8}$ erg cm $^{-2}$ s $^{-1}$ )							
	$F_{\text{diskbb}}$	$0.23^{+0.03}_{-0.03}$	$0.552^{+0.019}_{-0.028}$	$0.935^{+0.019}_{-0.023}$	$1.314^{+0.03}_{-0.017}$	$1.355^{+0.021}_{-0.025}$	$1.603^{+0.019}_{-0.022}$	$1.85^{+0.03}_{-0.05}$
	$F_{\text{relxillp}}$	$0.77^{+0.10}_{-0.06}$	$0.74^{+0.08}_{-0.08}$	$1.43^{+0.13}_{-0.11}$	$1.52^{+0.18}_{-0.12}$	$1.52^{+0.2}_{-0.12}$	$1.64^{+0.19}_{-0.14}$	$1.9^{+1.1}_{-0.5}$
	$F_{\text{cutoffpl}}$	$0.71^{+0.05}_{-0.07}$	$1.28^{+0.13}_{-0.15}$	$0.94^{+0.10}_{-0.20}$	$2.04^{+0.13}_{-0.21}$	$1.77^{+0.1}_{-0.12}$	$1.90^{+0.09}_{-0.27}$	$1.6^{+0.4}_{-0.3}$
	$L_{0.1-100\text{keV}}/L_{\text{Edd}}$ (%)	10.9	16.4	21.1	31.1	29.6	32.8	34.1
<b>constant</b>	ME/LE				$1.023^{+0.013}_{-0.014}$			
	HE/LE				$1.110^{+0.019}_{-0.023}$			
	$\chi^2/\text{d.o.f}$				3697.6/3384			

*Note.* Best-fit parameters for the model **tbabs\*(diskbb+relxillp+cutoffpl)**. Parameters with \* are fixed during the fit and the symbol  $P$  denotes the upper or lower boundary. Parameters that are only shown for Epoch 4 are tied across all observations. The flux of each spectral component is calculated in the 0.1–100 keV band using the **cflux** model. The absorption corrected X-ray flux ( $L_{0.1-100\text{keV}}$ ) is calculated with the **flux** command in **XSPEC**.

ilarly, in Jiang et al. (2019a), the intermediate state of GX 339–4 requires no distance reflection.

### 3.2.6. Comptonization of the reflection component

The power-law emission is the result of inverse Compton scattering of the disk photons by the hot electrons (but see Sridhar et al. 2021, 2022) in the corona. Some of the reflected emission should also intercept the corona and be Comptonized. Therefore, a self-consistent model should take the Comptonized reflection spectrum into account (Steiner et al. 2017; Wang-Ji et al. 2018). We consider this scenario with the Compton scattering kernel **simplcut** (Steiner et al. 2017). The full model reads as **tbabs\*simplcut\*(diskbb+relxillp)** (Model 3). The photon index ( $\Gamma$ ) and electron temperature ( $kT_e$ ) of **simplcut** are linked to the corresponding parameters in **relxillp**. There are two more parameters in the Compton scattering kernel: the reflection fraction  $R_f$  and the scattered fraction  $f_{\text{sc}}$ . We fix the reflection fraction parameter at the flux ratio between the reflection and power-law components in the 20–40 keV band derived from Model 2 and let the scattered fraction parameter free to vary.

With this model, we are assuming an equal fraction of the disk photons and the reflected photons are scattered by the corona. The best-fit parameters are shown in Tab. 6. We note that including the effect of Comptoniza-

tion of the disk and reflection photons does not change significantly the measurements of parameters like  $T_{\text{in}}$ ,  $\Gamma$  and  $R_{\text{in}}$ . The measurements of the spin and inclination parameters are also not affected. The scattered fraction decreases from 0.12 to 0.07, which may indicate changes of the disk-corona system during the transition.

### 3.2.7. The *refhidden* model

In the **relxill** model, the ionization balance on the disk is calculated using only the incident corona emission. In reality, we would expect that the thermal emission from the disk can also affect the ionization state. This is particularly important in XRBs since the disk temperature of XRBs can be very high ( $\sim 1$  keV) and the thermal emission can dominate the X-ray spectra. In some cases, the disk emission has been found to return to the disk and the reflection model assuming the primary continuum to be only a blackbody (García et al. 2022b) fits the data well (e.g. Connors et al. 2020, 2021). However, in the intermediate states, the strength of the disk and power-law components are comparable (see Fig. 3 and Tab. 1). As a consequence, considering only one of the components (disk or corona) to ionize the disk atmosphere is not appropriate.

Therefore, we implement the **refhidden** model that is specifically designed for accreting stellar mass black holes (Ross & Fabian 2007). In this model, the

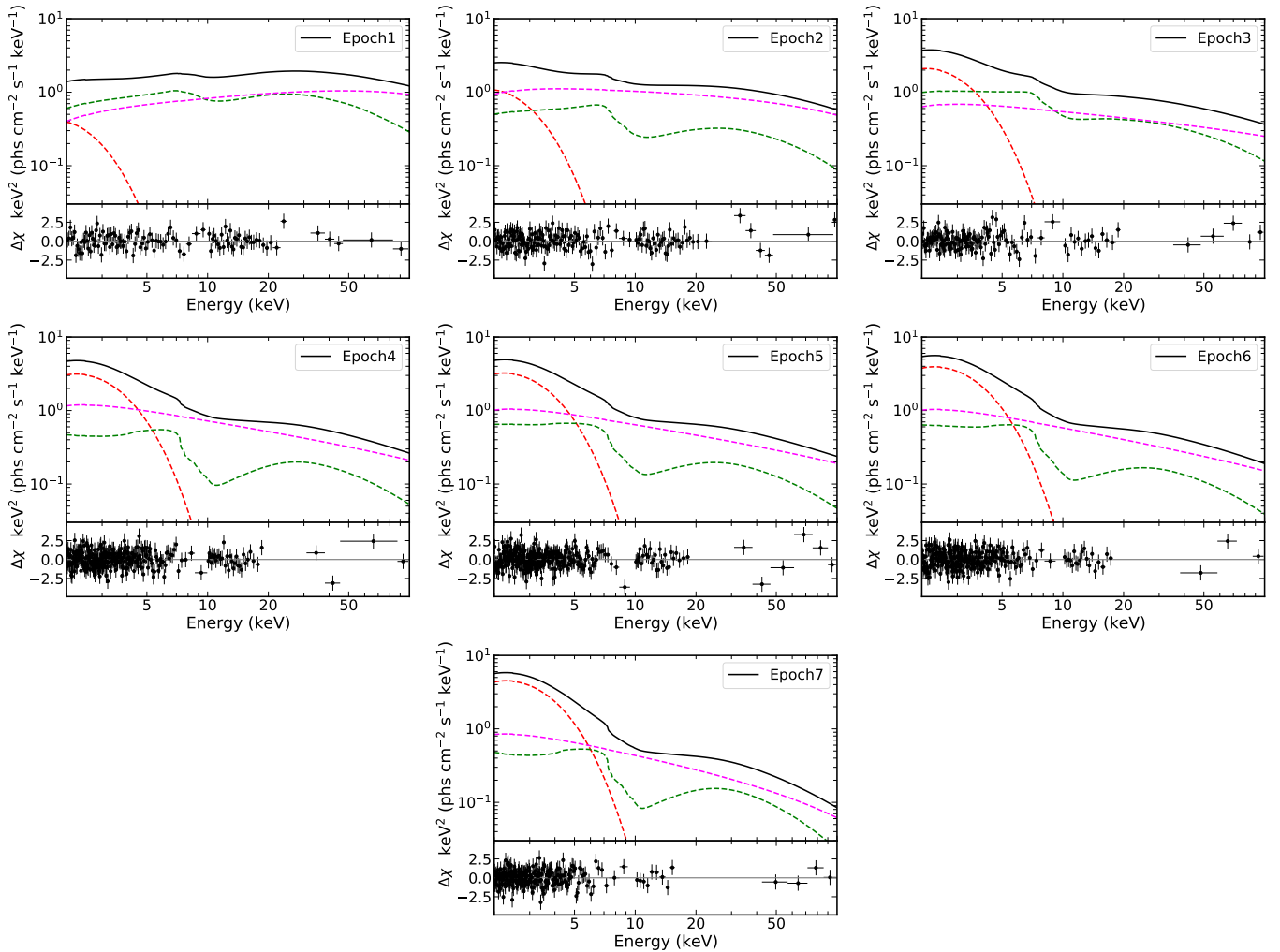


FIG. 3.— The best-fit model components for the seven epochs and the corresponding residuals with the model `tbabs*(diskbb+relxillp+cutoffpl)`. The black solid line represents the total model. The magenta, red and green dashed lines are for the corona emission, the disk component and the reflected component respectively.

disk atmosphere is ionized by the combination of a power-law component from above and a blackbody from below. Note that here the blackbody is assumed to be single-temperature, which is different from the multi-temperature disk blackbody component. The model also includes the effect of Comptonization in the accretion disk. The full model reads as `tbabs*simplcut*relconv*refhiden` (Model 4). The broadening kernel `relconv` (Dauser et al. 2010) is required to account for the relativistic effects. The disk thermal emission is already incorporated in `refhiden` so there is no need to add additional disk component. The parameters in the `refhiden` model include: the hydrogen number density on the disk ( $H_{\text{den}}$ ), the temperature of the blackbody from the disk ( $kT_{\text{bb}}$ ), the flux ratio between the power-law and blackbody components and the power-law index  $\Gamma$  (Illum/BB). We link  $\Gamma$  of the `refhiden` to the same parameter in `simplcut`. To better constrain the evolution of other parameters, we fix the black hole spin at 0.998 for the fitting.

The model provides an acceptable fit ( $\chi^2/\nu = 3788.8/3386$ ) and the best-fit parameters are shown in Tab. 7. The variations of spectral parameters from this model during the state transition are shown in the right

panels of Fig. 4 and can be compared with that from Model 1A in the left panels. The `refhiden` model gives a blackbody temperature ( $kT_{\text{bb}}$ ) that is systematically lower than the  $T_{\text{in}}$  found in other fits with the `diskbb` model. This is within expectation because the temperature in `refhiden` is the effective mid-plane temperature of the disk. The disk surface temperature would be higher after including the effect of color correction (see the discussion in Reis et al. 2008). Moreover, `diskbb` assumes a multi-temperature blackbody while a single temperature is used in `refhiden`. This is probably also affecting the value of the scattering fraction ( $f_{\text{sc}}$ ) of `simplcut` but the decreasing trend of this parameter along with the transition is retained. The number density of hydrogen is higher at the early phase of the transition (the first two epochs). One parameter of `refhiden` that clearly changes through the transition is the flux ratio between the illuminating power-law and the blackbody from the disk mid-plane.

## 4. DISCUSSION

### 4.1. Evolution of the disc-corona system

For the transition from the hard to the soft state, GX 339-4 gets progressively brighter in X-ray. In Fig. 4,

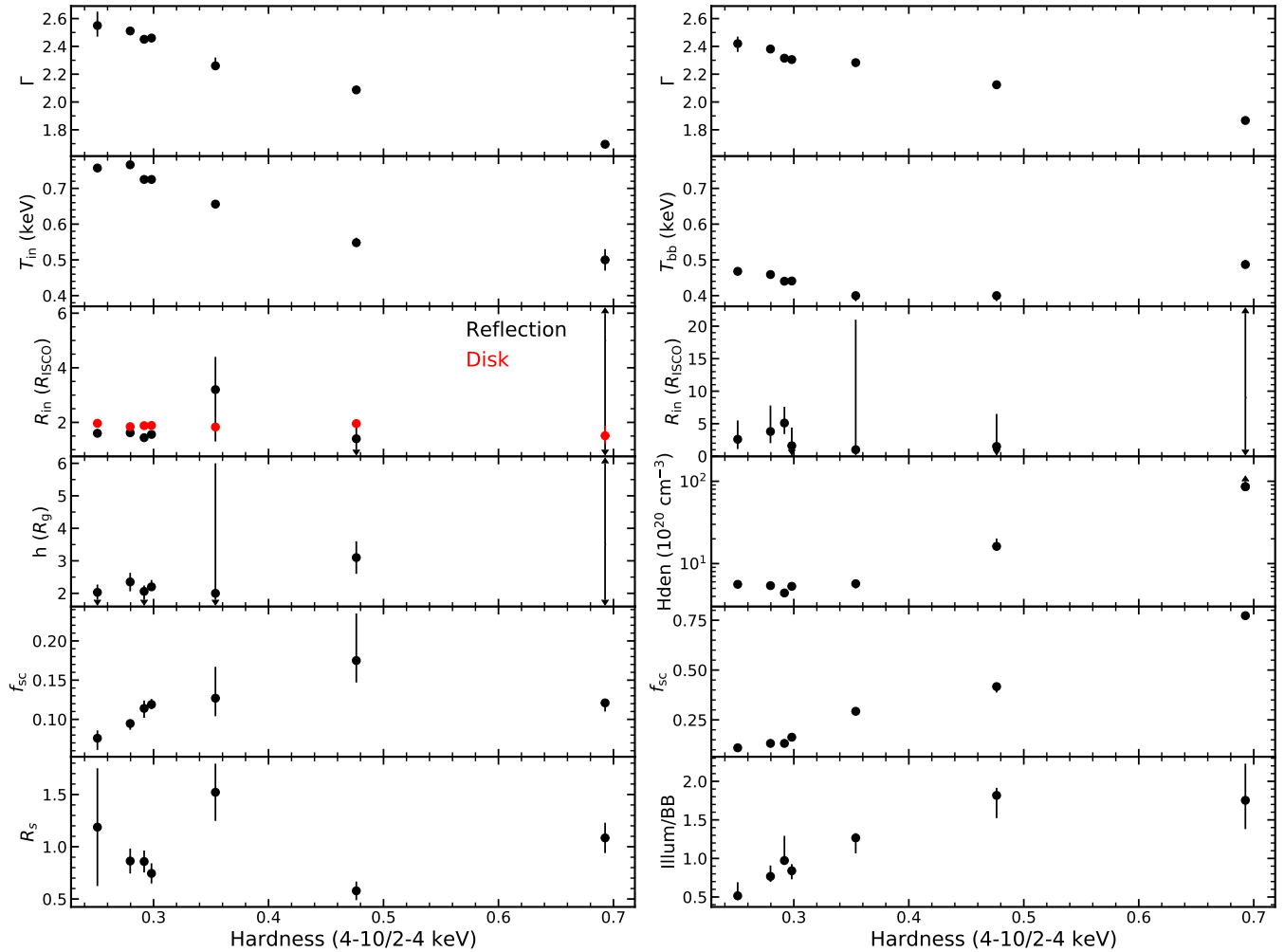


FIG. 4.— The evolution of spectral parameters along with X-ray hardness of the source. The definition of the hardness is the same as in Fig. 1. Lower and upper limits are marked with arrows. Panels in the left show the parameters from Model 1A except the scattering fraction ( $f_{sc}$ , from Model 3). In the third panel in the left, the red color represents estimation of the inner disk radius from the normalization parameter of `diskbb` of Model 3 and the size of the ISCO is chosen for a black hole with  $a_* = 0.95$ . The reflection strength ( $R_s$ ) is defined as the ratio between the observed flux of the reflected and the direct corona emission in the 0.1–100 keV band. Parameters from Model 4 and the `refhiden` model are shown in the right panels.

we show how the spectral parameters evolve with X-ray hardness of the source. The state transition can be characterized by decreasing of the hardness. This process is apparently associated with the steepening of the corona emission component, with a photon index ( $\Gamma$ ) evolving from 1.7 to 2.5 (see the top panel of Fig. 4). Meanwhile, the X-ray luminosity increases from 10% to 20% of the Eddington limit assuming a black hole mass of  $10 M_\odot$  and a distance of 8 kpc (see Tab. 5). There is a clear trend of the inner disk temperature increasing from 0.5 to 0.76 keV. The contribution of the disk component (in 0.1–100 keV band) also increases from 13% to 35%. This increase of soft cooling photons could explain the softening of the corona emission (e.g. Del Santo et al. 2008).

As for the coronal temperature ( $kT_e$ ), the data do not provide good constraint on this parameter. Only lower limits are found for Epoch 2–7 (see Tab. 5), while these lower limits are still higher than the measurement of Epoch 1. This weak tendency of increasing coronal temperature during the state transition is consistent with previous broadband spectral analysis of GX 339-4 (e.g. Motta et al. 2009; Sridhar et al. 2020) and other systems

(e.g. Zhang et al. 2022). It is different from the tendency of decreasing coronal temperature with luminosity in the hard state (e.g. García et al. 2015) which is thought to be a result of stronger cooling by the seed photons. What is happening in the state transition could be that the decrease of the optical depth (e.g. McConnell et al. 2002; Del Santo et al. 2008) causes less scattering between the seed photons and corona electrons and then increases the coronal temperature. Note that this increase of coronal temperature will be limited by the run-away electron-positron pair production process in the corona (e.g. Fabian et al. 2015).

Another parameter that is of interest is the inner radius of the accretion disk ( $R_{in}$ ). There are already reflection-based studies that have investigated the accretion geometry of GX 339-4 in the hard state. In García et al. (2015), the luminosity range from 1.7% to 17% of the Eddington limit ( $L_{Edd}$ ) has been studied with data from *RXTE*/PCA and the  $R_{in}$  is found to be close to the ISCO ( $< 5 R_{ISCO}$ ). Plant et al. (2015) have studied similar luminosity levels with data from *XMM-Newton* in the timing mode but found large truncations of the

disk (see also Basak & Zdziarski 2016). This discrepancy could be due to the complex pile-up effect in the timing mode that can affect the iron K line (e.g. Miller et al. 2010). The regime below 1% of the Eddington luminosity has also been studied with reflection models (e.g. Shidatsu et al. 2011; Petrucci et al. 2014; Wang-Ji et al. 2018; Wang et al. 2020). These studies indicate that  $R_{\text{in}}$  should decrease with increasing luminosity and reaches  $20 R_g$  when the luminosity is above 1% Eddington (see Fig. 6 of García et al. 2019).

Our analysis concerns the reflection spectra of GX 339–4 during the hard-to-soft transition that covers the luminosity range from 10% to 20%  $L_{\text{Edd}}$ . The results show that  $R_{\text{in}}$  is not constrained in Epoch 1. This is probably because of the low statistics of the data since Epoch 1 has the shortest exposure among all epochs. After Epoch 2,  $R_{\text{in}}$  is consistent with the ISCO in some models and still below a few times the ISCO in other models. This indicates that the disk inner edge is relatively stable across the state transition.<sup>10</sup> The inner disc radius can also be estimated from the normalization parameter of the `diskbb` model (Kubota et al. 1998). We use values from Model 3 since it takes into account both the transmitted and scattered disk photons. The results are shown in Fig. 4 in red assuming a distance of 8 kpc, a black hole mass of  $10 M_{\odot}$ , an inclination of 40 deg, a color correction factor of 1.7 and a relativistic correction factor of 0.412. It again shows that the inner disk radius is stable through the transition although the absolute values need to be taken with caution as there are systematic uncertainties in the assumptions for mass, distance and color correction.

Similar results have been found by Sridhar et al. (2020) who studies the 2002–2003 and 2004–2005 outbursts of GX 339–4 with data from *RXTE*/PCA. In their work, by fixing the black hole spin at 0.998, the  $R_{\text{in}}$  is found to reach close to the ISCO at the onset of the transition for both outbursts even though the transition luminosity differs by a factor of 3. A stable disk during the state transition has also been found in other systems (e.g. XTE J1550–564, Rodríguez et al. 2003; MAXI J1820+070, Wang et al. 2021).

The corona height shows similar tendency as  $R_{\text{in}}$ , which is not constrained in Epoch 1 and remains close to the black hole ( $< 6 R_g$ ) in the following observations. When the primary source is close to the black hole, the light bending effect would concentrate its radiation to the innermost part of the accretion disk (e.g. Dauser et al. 2013). This is indeed what we find with the broken power-law emissivity, with which we obtain a steep inner emissivity index (see Tab. 3). We also define an empirical reflection strength parameter ( $R_s$ ) which is the ratio between the reflected and the power-law flux in the 0.1–100 keV band. This is different from but similar to the reflection fraction parameter ( $R_f$ ), which is the ratio between the corona intensity that illuminates the disk and the corona intensity that reaches the observer (Dauser et al. 2016). Variation of the reflection strength may indicate changes of the disk-corona system (e.g. You et al.

2021). The lowest panel in the left of Fig. 4 shows no significant changes of this parameter, which is consistent with the prediction of a stable inner disk radius.

We note that relativistic reflection analysis based on the single lamppost geometry may only be sensitive to the parts of the corona that are close to the black hole since they dominate the reflection emissivity (see Wang et al. 2021). In practice, the two-lamppost reflection models have been used to mimic a vertically extended corona (e.g. Buisson et al. 2019). The upper lamppost could be responsible for the narrow cores in the iron band that is usually assumed to originate from a distant reflector (e.g. García et al. 2019). We do not explore further in this aspect since our data does not require the presence of a narrow iron line.

The scattering fraction parameter ( $f_{\text{sc}}$ ) in `simplcut` is related to the geometry of the disk-corona system and also the optical depth of the corona. From Fig. 4, we see that, except for Epoch 1,  $f_{\text{sc}}$  from Model 3 shows a tentative decreasing trend through the transition although the uncertainties are large. The trend is more evident in Model 4 (see the right panel of Fig. 4). In the fit with `reftiden`, we find that the flux ratio between the illuminating power-law component and the blackbody component from the disk (Illum/BB) also decreases by a factor of 3 from Epoch 1 to Epoch 7. Meanwhile, the temperature of the disk mid-plane ( $T_{\text{bb}}$ ) only changes in a narrow range (0.4–0.5 keV). Given these variation patterns and the fact that the inner disk radius remains stable, we argue that the state transition is more likely to be related to the corona properties instead of the inner edge of the disk. This scenario is also supported by recent studies on the reverberation lag of black hole transients (Wang et al. 2022), in which the lag is found to become longer across the hard-to-soft transition and is explained as a vertically expanding jet. Similar corona behavior has also been found in other sources by analyzing the lag spectrum with Comptonization models (e.g. García et al. 2021, 2022a; Méndez et al. 2022; Zhang et al. 2022; Peirano et al. 2023).

The ionization parameter  $\xi$  is defined as  $\xi = L/nr^2$  where  $L$  is the ionizing luminosity,  $n$  is the density and  $r$  is the distance to the illuminating source. We do not see strong variation on the ionization parameter. This is within our expectation since the source luminosity changes by only a factor of 2. The variation of the ionization parameter would be comparable to its fitting uncertainties if the density and distance do not change. Among the seven epochs, a high ionization parameter ( $\log(\xi) > 3.6$ ) is always required to fit the reflection spectra. This high ionization state is consistent with previous studies of GX 339–4 at similar luminosity levels (e.g. Sridhar et al. 2020). With the measured ionization parameter and the known source luminosity, we can calculate the disk density and compare it with our measurements (e.g. Tab. 4). Using the Equ. 9 of Zdziarski & De Marco (2020), we calculate a disk density of  $n_{\text{cal}} \sim 10^{22} \text{ cm}^{-3}$  with the averaged illuminating flux and ionization parameter in Tab. 4. This value is higher than what we measured with the `relxillD` model and exceeds the upper limit ( $10^{19} \text{ cm}^{-3}$ )<sup>11</sup> allowed by the model. Similar discrepancy has been found in other in-

<sup>10</sup> We note that the *Insight*-HXMT spectra of this outburst in the bright hard state ( $> 8\% L_{\text{Edd}}$ , before our Epoch 1) have also been analyzed and the inner radius is found to be constant ( $\sim 3 R_{\text{ISCO}}$ , Ren et al. in prep).

<sup>11</sup> Note that in the latest version of `relxill`, which was re-



intermediate data of GX 339–4 (e.g. [Zdziarski & De Marco 2020](#)). It might be explained if the inner disk radius is 30 times larger than the ISCO but it would conflict with the broad iron line we are seeing. More work in developing the reflection models would help to better understand this problem.

#### 4.2. Measurement of system parameters

By fitting the seven spectra simultaneously with relativistic reflection models, we are able to measure the black hole spin parameter of GX 339–4. We obtain a constraint of  $a_* > 0.95$  if assuming a lamppost geometry. When implementing a broken power-law emissivity in `relxill`, we obtain the lowest  $\chi^2$  among all models and get a constraint of  $a_* > 0.86$  (see Fig. 5). This measurement confirms the high spin nature of the black hole in GX 339–4 as found in previous studies with data in the hard (e.g. [Reis et al. 2008](#); [Ludlam et al. 2015](#); [García et al. 2015](#)) or soft states (e.g. [Parker et al. 2016](#)).

Previous reflection based analysis have constrained the disk inclination angle of GX 339–4 to be  $30^\circ$ – $60^\circ$  (e.g. [García et al. 2015](#); [Parker et al. 2016](#)). Moreover, by studying the near-infrared lightcurve of GX 339–4, [Heida et al. \(2017\)](#) have measured the orbital inclination to be  $37^\circ$ – $78^\circ$ . A more recent work by [Zdziarski et al. \(2019\)](#) updated the inclination to  $\approx 40^\circ$ – $60^\circ$  based on considering evolutionary models for the donor. Our measurement of the inclination angle of the inner accretion disk ranges from 35 to 43 degree, which is consistent with the previous studies via different methods. We also find that the constraint on the inclination with reflection spectroscopy slightly changes ( $42.0^{+1.3}_{-1.4}$  with the lamppost geometry and  $36.6^{+1.5}_{-1.3}$  for the broken power-law emissivity) with the treatments of the emissivity profile (see Fig. 5). These differences on parameter measurements due to systematic uncertainties are expected for reflection spectroscopy (e.g. [Zhou et al. 2020](#); [Cárdenas-Avendaño et al. 2020](#)). It is a result of the lack of our knowledge about the system. We note that these systematic uncertainties should be considered when reporting measurements of parameters with disk reflection models. Other sources of systematic uncertainties include simplifications in the models (e.g. the discussion in [Tripathi et al. 2021](#)) or instrumental effects (see the review in [Bambi et al. 2021](#)).

We always obtain a very high iron abundance that is near ten times of the solar value. We note that the measurement may not represent the true abundance of the system. The super-solar iron abundance is a well known issue in the fitting of the relativistic reflection features (e.g. [Dauser et al. 2012](#); [Jiang et al. 2018](#); [García et al. 2018](#)). It has been shown that allowing the electron density ( $n_e$ ) of the disk to go higher than what is assumed in the standard reflection model ( $\log(n_e/\text{cm}^{-3})=15$ ) could help to lower the iron abundance (e.g. [Tomsick et al. 2018](#); [Jiang et al. 2019a](#)). However, our high-density model still gives a very high iron abundance ( $A_{\text{Fe}} > 8.6$ ).

Another solution to solve this high iron abundance problem is to allow different photon indexes for the directly observed primary emission and the reflection spectrum (e.g. [Füerst et al. 2015](#)). We test this scenario but it does not help to lower the iron abundance (with  $A_{\text{Fe}} > 9.0$ ). We note that the corona structure may be more complex than two uniform clouds of plasma (e.g. [Uttley et al. 2011](#)). Moreover, [Ross et al. \(2002\)](#) have found that ignoring the returning radiation could also affect the measurement of the iron abundance while more recent studies on the returning radiation do not find strong impact (e.g. [Riaz et al. 2021](#); [Dauser et al. 2022](#)). There is also the possibility that the high iron abundance is real and caused by radiative levitation of metal ions in the inner part of the accretion disk (e.g. [Reynolds et al. 2012](#)).

## 5. CONCLUSION

In this work, we analyzed the broadband spectra (2–100 keV) of GX 339–4 during the bright state transition of its 2021 outburst observed by *Insight*–HXMT. Strong relativistic reflection features were found in the spectra, which allowed us to study the evolution of the disk-corona system during the transition. The main results are the following:

- The hard to soft transition is associated with a stronger contribution of the disk thermal component to the X-ray spectrum and a steepening of the power-law emission.
- The inner disk radius stays close to the ISCO during the transition. This is even true when we consider a reflection model that assumes the ionizing continuum to be a combination of the corona emission from above and a blackbody emission from below.
- If assuming a lamppost geometry, the measured corona height is always close to the black hole.
- The scattering fraction, which is the fraction of the disk photons that are scattered by the hot corona, decreases along with the transition.
- The data provide constraint on the black hole spin ( $a_* > 0.86$ ) and the inclination parameter ( $i \approx 35^\circ$ – $43^\circ$ ) of the system.

**Acknowledgments** – We thank the anonymous referee for helpful comments to improve the manuscript. We thank Yuexin Zhang for useful discussion. This work was supported by the National Natural Science Foundation of China (NSFC), Grant No. 11973019 and Grant No. 12250610185, the Natural Science Foundation of Shanghai, Grant No. 22ZR1403400, the Shanghai Municipal Education Commission, Grant No. 2019-01-07-00-07-E00035, and Fudan University, Grant No. JIH1512604. JJ acknowledges support from the Leverhulme Trust, the Isaac Newton Trust and St Edmund’s College.

## REFERENCES

- Arnaud, K. A. 1996, in *Astronomical Society of the Pacific Conference Series*, Vol. 101, *Astronomical Data Analysis Software and Systems V*, ed. G. H. Jacoby & J. Barnes, 17
- Bambi, C. 2017, *Reviews of Modern Physics*, 89, 025001

leased after writing of this paper, the density is allowed to vary up to  $10^{20} \text{ cm}^{-3}$ . See <http://www.sternwarte.uni-erlangen.de/~dauser/research/relxill/>.

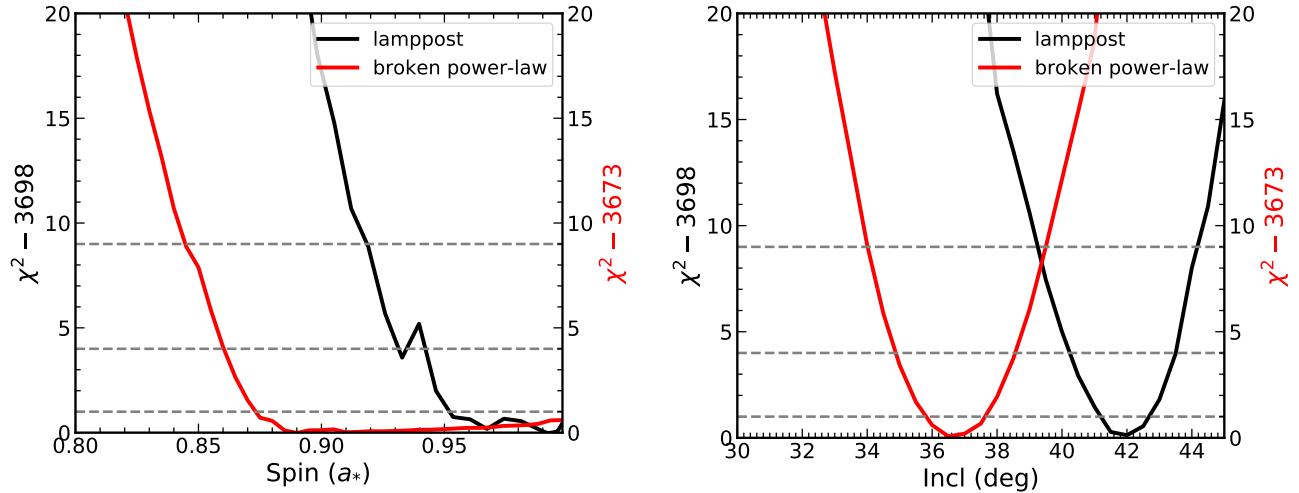


FIG. 5.— The  $\chi^2$  contours for the black hole spin and the inclination parameters for the lamppost geometry and broken power-law emissivity. The horizontal lines represent the  $1\sigma$ ,  $2\sigma$  and  $3\sigma$  confidence levels for a single parameter of interest.

- Bambi, C., Brenneman, L. W., Dauser, T., et al. 2021, *Space Sci. Rev.*, 217, 65
- Basak, R., & Zdziarski, A. A. 2016, *MNRAS*, 458, 2199
- Belloni, T., Homan, J., Casella, P., et al. 2005, *A&A*, 440, 207
- Belloni, T., Parolin, I., Del Santo, M., et al. 2006, *MNRAS*, 367, 1113
- Belloni, T. M. 2010, in *Lecture Notes in Physics*, Berlin Springer Verlag, ed. T. Belloni, Vol. 794, 53
- Buisson, D. J. K., Fabian, A. C., Barret, D., et al. 2019, *MNRAS*, 490, 1350
- Cao, X., Jiang, W., Meng, B., et al. 2020, *Science China Physics, Mechanics, and Astronomy*, 63, 249504
- Cárdenas-Avendaño, A., Zhou, M., & Bambi, C. 2020, *Phys. Rev. D*, 101, 123014
- Chen, Y., Cui, W., Li, W., et al. 2020, *Science China Physics, Mechanics, and Astronomy*, 63, 249505
- Connors, R. M. T., García, J. A., Dauser, T., et al. 2020, *ApJ*, 892, 47
- Connors, R. M. T., García, J. A., Tomsick, J., et al. 2021, *ApJ*, 909, 146
- Dauser, T., García, J., Walton, D. J., et al. 2016, *A&A*, 590, A76
- Dauser, T., García, J., Wilms, J., et al. 2013, *MNRAS*, 430, 1694
- Dauser, T., García, J. A., Joyce, A., et al. 2022, *MNRAS*, 514, 3965
- Dauser, T., Wilms, J., Reynolds, C. S., & Brenneman, L. W. 2010, *MNRAS*, 409, 1534
- Dauser, T., Svoboda, J., Schartel, N., et al. 2012, *MNRAS*, 422, 1914
- Del Santo, M., Malzac, J., Jourdain, E., Belloni, T., & Ubertini, P. 2008, *MNRAS*, 390, 227
- Done, C., Gierliński, M., & Kubota, A. 2007, *A&A Rev.*, 15, 1
- Dove, J. B., Wilms, J., & Begelman, M. C. 1997, *ApJ*, 487, 747
- Dzielał, M. A., Zdziarski, A. A., Szanecki, M., et al. 2019, *MNRAS*, 485, 3845
- Esin, A. A., McClintock, J. E., & Narayan, R. 1997, *ApJ*, 489, 865
- Fabian, A. C., Iwasawa, K., Reynolds, C. S., & Young, A. J. 2000, *PASP*, 112, 1145
- Fabian, A. C., Lohfink, A., Kara, E., et al. 2015, *MNRAS*, 451, 4375
- Fabian, A. C., Parker, M. L., Wilkins, D. R., et al. 2014, *MNRAS*, 439, 2307
- Fabian, A. C., Rees, M. J., Stella, L., & White, N. E. 1989, *MNRAS*, 238, 729
- Fender, R. P., Belloni, T. M., & Gallo, E. 2004, *MNRAS*, 355, 1105
- Fürst, F., Nowak, M. A., Tomsick, J. A., et al. 2015, *ApJ*, 808, 122
- García, F., Karpouzas, K., Méndez, M., et al. 2022a, *MNRAS*, 513, 4196
- García, F., Méndez, M., Karpouzas, K., et al. 2021, *MNRAS*, 501, 3173
- García, J., Dauser, T., Reynolds, C. S., et al. 2013, *ApJ*, 768, 146
- García, J., & Kallman, T. R. 2010, *ApJ*, 718, 695
- García, J., Dauser, T., Lohfink, A., et al. 2014, *ApJ*, 782, 76
- García, J. A., Dauser, T., Ludlam, R., et al. 2022b, *ApJ*, 926, 13
- García, J. A., Fabian, A. C., Kallman, T. R., et al. 2016, *MNRAS*, 462, 751
- García, J. A., Kallman, T. R., Bautista, M., et al. 2018, in *Astronomical Society of the Pacific Conference Series*, Vol. 515, *Workshop on Astrophysical Opacities*, 282
- García, J. A., Steiner, J. F., McClintock, J. E., et al. 2015, *ApJ*, 813, 84
- García, J. A., Tomsick, J. A., Sridhar, N., et al. 2019, *ApJ*, 885, 48
- George, I. M., & Fabian, A. C. 1991, *MNRAS*, 249, 352
- Gierliński, M., & Done, C. 2004, *MNRAS*, 347, 885
- Guo, C.-C., Liao, J.-Y., Zhang, S., et al. 2020, *Journal of High Energy Astrophysics*, 27, 44
- Heida, M., Jonker, P. G., Torres, M. A. P., & Chiavassa, A. 2017, *ApJ*, 846, 132
- Homan, J., & Belloni, T. 2005, *Ap&SS*, 300, 107
- Jiang, J., Fabian, A. C., Wang, J., et al. 2019a, *MNRAS*, 484, 1972
- Jiang, J., Parker, M. L., Fabian, A. C., et al. 2018, *MNRAS*, 477, 3711
- Jiang, J., Fabian, A. C., Dauser, T., et al. 2019b, *MNRAS*, 489, 3436
- Joinet, A., Kalemci, E., & Senziani, F. 2008, *ApJ*, 679, 655
- Kubota, A., Tanaka, Y., Makishima, K., et al. 1998, *PASJ*, 50, 667
- Liao, J.-Y., Zhang, S., Lu, X.-F., et al. 2020a, *Journal of High Energy Astrophysics*, 27, 14
- Liao, J.-Y., Zhang, S., Chen, Y., et al. 2020b, *Journal of High Energy Astrophysics*, 27, 24
- Liu, C., Zhang, Y., Li, X., et al. 2020, *Science China Physics, Mechanics, and Astronomy*, 63, 249503
- Liu, H., Abdikamalov, A. B., Ayzenberg, D., et al. 2019, *Phys. Rev. D*, 99, 123007
- Liu, H., Jiang, J., Zhang, Z., et al. 2022, *MNRAS*, 513, 4308
- Ludlam, R. M., Miller, J. M., & Cackett, E. M. 2015, *ApJ*, 806, 262
- Mahmoud, R. D., Done, C., & De Marco, B. 2019, *MNRAS*, 486, 2137
- McConnell, M. L., Zdziarski, A. A., Bennett, K., et al. 2002, *ApJ*, 572, 984
- Méndez, M., Karpouzas, K., García, F., et al. 2022, *Nature Astronomy*, 6, 577
- Miller, J. M., Fabian, A. C., Reynolds, C. S., et al. 2004, *ApJ*, 606, L131
- Miller, J. M., D’Ai, A., Bautz, M. W., et al. 2010, *ApJ*, 724, 1441
- Miller, J. M., Parker, M. L., Fuerst, F., et al. 2013, *ApJ*, 775, L45
- Mitsuda, K., Inoue, H., Koyama, K., et al. 1984, *PASJ*, 36, 741

- Miyakawa, T., Yamaoka, K., Homan, J., et al. 2008, PASJ, 60, 637
- Motta, S., Belloni, T., & Homan, J. 2009, MNRAS, 400, 1603
- Narayan, R. 2005, Ap&SS, 300, 177
- Parker, M. L., Tomsick, J. A., Kennea, J. A., et al. 2016, ApJ, 821, L6
- Peirano, V., Méndez, M., García, F., & Belloni, T. 2023, MNRAS, 519, 1336
- Petrucci, P. O., Cabanac, C., Corbel, S., Koerding, E., & Fender, R. 2014, A&A, 564, A37
- Plant, D. S., Fender, R. P., Ponti, G., Muñoz-Darias, T., & Coriat, M. 2015, A&A, 573, A120
- Reis, R. C., Fabian, A. C., Ross, R. R., et al. 2008, MNRAS, 387, 1489
- Remillard, R. A., & McClintock, J. E. 2006, ARA&A, 44, 49
- Reynolds, C. S. 2014, Space Sci. Rev., 183, 277
- Reynolds, C. S., Brenneman, L. W., Lohfink, A. M., et al. 2012, ApJ, 755, 88
- Riaz, S., Szanecki, M., Niedźwiecki, A., Ayzenberg, D., & Bambi, C. 2021, ApJ, 910, 49
- Rodriguez, J., Corbel, S., & Tomsick, J. A. 2003, ApJ, 595, 1032
- Ross, R. R., & Fabian, A. C. 2007, MNRAS, 381, 1697
- Ross, R. R., Fabian, A. C., & Ballantyne, D. R. 2002, MNRAS, 336, 315
- Ross, R. R., Fabian, A. C., & Young, A. J. 1999, MNRAS, 306, 461
- Shakura, N. I., & Sunyaev, R. A. 1973, A&A, 24, 337
- Shidatsu, M., Ueda, Y., Tazaki, F., et al. 2011, PASJ, 63, S785
- Sridhar, N., García, J. A., Steiner, J. F., et al. 2020, ApJ, 890, 53
- Sridhar, N., Sironi, L., & Beloborodov, A. M. 2021, MNRAS, 507, 5625
- . 2022, MNRAS, arXiv:2203.02856
- Steiner, J. F., García, J. A., Eikmann, W., et al. 2017, ApJ, 836, 119
- Steiner, J. F., McClintock, J. E., Remillard, R. A., et al. 2010, ApJ, 718, L117
- Szanecki, M., Niedźwiecki, A., Done, C., et al. 2020, A&A, 641, A89
- Tomsick, J. A., Kaaret, P., Kroeger, R. A., & Remillard, R. A. 1999, ApJ, 512, 892
- Tomsick, J. A., Yamaoka, K., Corbel, S., et al. 2009, ApJ, 707, L87
- Tomsick, J. A., Parker, M. L., García, J. A., et al. 2018, ApJ, 855, 3
- Tripathi, A., Zhang, Y., Abdikamalov, A. B., et al. 2021, ApJ, 913, 79
- Uttley, P., Wilkinson, T., Cassatella, P., et al. 2011, MNRAS, 414, L60
- Verner, D. A., Ferland, G. J., Korista, K. T., & Yakovlev, D. G. 1996, ApJ, 465, 487
- Wang, J., Kara, E., Steiner, J. F., et al. 2020, ApJ, 899, 44
- Wang, J., Mastroserio, G., Kara, E., et al. 2021, ApJ, 910, L3
- Wang, J., Kara, E., Lucchini, M., et al. 2022, ApJ, 930, 18
- Wang-Ji, J., García, J. A., Steiner, J. F., et al. 2018, ApJ, 855, 61
- Wilkins, D. R., & Gallo, L. C. 2015, MNRAS, 449, 129
- Wilms, J., Allen, A., & McCray, R. 2000, ApJ, 542, 914
- Yamaoka, K., Uzawa, M., Arai, M., Yamazaki, T., & Yoshida, A. 2005, Chinese Journal of Astronomy and Astrophysics Supplement, 5, 273
- Yan, Z., Xie, F.-G., & Zhang, W. 2020, ApJ, 889, L18
- You, B., Tuo, Y., Li, C., et al. 2021, Nature Communications, 12, 1025
- Zdziarski, A. A., & De Marco, B. 2020, ApJ, 896, L36
- Zdziarski, A. A., De Marco, B., Szanecki, M., Niedźwiecki, A., & Markowitz, A. 2021, ApJ, 906, 69
- Zdziarski, A. A., & Gierliński, M. 2004, Progress of Theoretical Physics Supplement, 155, 99
- Zdziarski, A. A., Johnson, W. N., & Magdziarz, P. 1996, MNRAS, 283, 193
- Zdziarski, A. A., Ziółkowski, J., & Mikołajewska, J. 2019, MNRAS, 488, 1026
- Zhang, S., Lu, F. J., Zhang, S. N., & Li, T. P. 2014, in Society of Photo-Optical Instrumentation Engineers (SPIE) Conference Series, Vol. 9144, Space Telescopes and Instrumentation 2014: Ultraviolet to Gamma Ray, ed. T. Takahashi, J.-W. A. den Herder, & M. Bautz, 914421
- Zhang, S.-N., Li, T., Lu, F., et al. 2020, Science China Physics, Mechanics, and Astronomy, 63, 249502
- Zhang, Y., Méndez, M., García, F., et al. 2022, MNRAS, 512, 2686
- Zhou, M., Ayzenberg, D., Bambi, C., & Nampalliwar, S. 2020, Phys. Rev. D, 101, 043010
- Życki, P. T., Done, C., & Smith, D. A. 1999, MNRAS, 309, 561

## APPENDIX

## THE HXMT OBSERVATIONS

## THE BEST-FIT TABLES

TABLE 2  
*Insight*–HXMT OBSERVATIONS OF GX 339–4 ANALYZED IN THIS PAPER

Reference name	Date <sup>1</sup>	obsID	Exposure (ks)			Start time	Stop time
			LE	ME	HE	MJD	MJD
Epoch 1	20210325	P030402403702	1.86	3.31	2.30	59298.012	59298.151
		P030402403703				59298.151	59298.289
Epoch 2	20210326	P030402403801	3.46	5.75	7.95	59299.602	59299.776
		P030402403802				59299.776	59299.909
		P030402403803				59299.909	59300.003
Epoch 3	20210327	P030402403901	2.40	3.86	3.88	59300.796	59300.923
		P030402403902				59300.923	59301.059
Epoch 4	20210328	P030402403903	7.25	12.9	13.2	59301.059	59301.204
		P030402403904				59301.204	59301.343
		P030402403905				59301.343	59301.498
		P030402403906				59301.498	59301.634
		P030402403907				59301.634	59301.794
		P030402403908				59301.794	59301.916
		P030402403909				59301.916	59302.052
Epoch 5	20210329	P030402403910	7.46	13.3	13.6	59302.052	59302.189
		P030402403911				59302.189	59302.347
		P030402403912				59302.347	59302.515
		P030402403913				59302.515	59302.648
		P030402403914				59302.648	59302.787
		P030402403915				59302.787	59302.961
		P030402403916				59302.961	59303.120
Epoch 6	20210330	P030402403917	5.63	11.2	11.4	59303.120	59303.260
		P030402403918				59303.260	59303.399
		P030402403919				59303.399	59303.551
		P030402403920				59303.551	59303.684
		P030402403921				59303.684	59303.816
		P030402403922				59303.816	59303.949
		P030402403923				59303.949	59304.081
Epoch 7	20210331	P030402403924	4.57	9.95	10.2	59304.081	59304.214
		P030402403925				59304.214	59304.346
		P030402403926				59304.346	59304.479
		P030402403927				59304.479	59304.611
		P030402403928				59304.611	59304.743
		P030402403929				59304.743	59304.876
		P030402403930				59304.876	59305.037

*Note.* (1) The observation date is presented in the form of `yyyymmdd`.



TABLE 3  
BEST-FIT VALUES WITH A BROKEN POWER-LAW EMISSIVITY WITH  $q_{\text{out}} = 3$  (MODEL 1B).

Component	Parameter	Epoch 1	Epoch 2	Epoch 3	Epoch 4	Epoch 5	Epoch 6	Epoch 7
<b>tbabs</b>	$N_{\text{H}}$ ( $10^{22}$ cm $^{-2}$ )				$0.99^{+0.05}_{-0.06}$			
<b>diskbb</b>	$T_{\text{in}}$ (keV)	$0.50^{+0.04}_{-0.04}$	$0.540^{+0.013}_{-0.012}$	$0.658^{+0.009}_{-0.009}$	$0.718^{+0.008}_{-0.011}$	$0.726^{+0.01}_{-0.011}$	$0.765^{+0.009}_{-0.008}$	$0.752^{+0.011}_{-0.009}$
<b>relxill</b>	$a_*$				$> 0.86$			
	$q_{\text{in}}$	3*	3*	3*	$10^{+P}_{-3}$	$10^{+P}_{-4}$	$9^{+P}_{-4}$	$7.4^{+P}_{-1.7}$
	$q_{\text{out}}$				3*			
	$R_{\text{br}}$ ( $R_{\text{g}}$ )	-	-	-	$3.5^{+0.5}_{-0.3}$	$3.6^{+0.8}_{-0.3}$	$3.62^{+1.3}_{-0.28}$	$4.2^{+0.9}_{-0.9}$
	Incl				$36.6^{+1.5}_{-1.3}$			
	$A_{\text{Fe}}$ (solar)				$10.0^{+P}_{-1.1}$			
	$R_{\text{in}}$ (ISCO)	$40^{+P}_{-33}$	$3.6^{+4.0}_{-1.6}$	$2.3^{+1.4}_{-0.6}$	$1.0^{+0.8}_{-P}$	$1.0^{+0.6}_{-P}$	$1.1^{+0.9}_{-P}$	$1.0^{+0.7}_{-P}$
	$\log(\xi)$	$4.29^{+0.05}_{-0.1}$	$4.54^{+0.05}_{-0.07}$	$4.60^{+0.07}_{-0.1}$	$4.02^{+0.21}_{-0.15}$	$4.35^{+0.12}_{-0.22}$	$4.31^{+0.14}_{-0.16}$	$4.1^{+0.3}_{-0.3}$
<b>cutoffpl</b>	$\Gamma$	$1.701^{+0.029}_{-0.025}$	$2.054^{+0.017}_{-0.013}$	$2.27^{+0.04}_{-0.06}$	$2.42^{+0.04}_{-0.04}$	$2.42^{+0.03}_{-0.04}$	$2.504^{+0.027}_{-0.027}$	$2.48^{+0.15}_{-0.1}$
	$E_{\text{cut}}$ (keV)	$140^{+30}_{-20}$	$> 450$	$> 400$	$> 220$	$> 330$	$> 410$	$130^{+70}_{-60}$
<b>cflux</b>								
$F_{\text{diskbb}}$	( $10^{-8}$ erg cm $^{-2}$ s $^{-1}$ )	$0.219^{+0.03}_{-0.024}$	$0.556^{+0.020}_{-0.029}$	$0.93^{+0.04}_{-0.03}$	$1.310^{+0.023}_{-0.025}$	$1.360^{+0.03}_{-0.023}$	$1.597^{+0.022}_{-0.025}$	$1.85^{+0.04}_{-0.06}$
$F_{\text{relxill}}$	( $10^{-8}$ erg cm $^{-2}$ s $^{-1}$ )	$0.73^{+0.16}_{-0.13}$	$1.26^{+0.07}_{-0.08}$	$1.44^{+0.17}_{-0.19}$	$1.38^{+0.14}_{-0.12}$	$1.45^{+0.11}_{-0.18}$	$1.62^{+0.2}_{-0.16}$	$1.56^{+0.5}_{-0.29}$
$F_{\text{cutoffpl}}$	( $10^{-8}$ erg cm $^{-2}$ s $^{-1}$ )	$0.73^{+0.07}_{-0.20}$	$0.57^{+0.15}_{-0.12}$	$0.9^{+0.5}_{-0.3}$	$1.78^{+0.25}_{-0.24}$	$1.52^{+0.22}_{-0.25}$	$1.80^{+0.23}_{-0.4}$	$1.3^{+0.6}_{-0.4}$
<b>constant</b>	ME/LE				$1.035^{+0.014}_{-0.014}$			
	HE/LE				$1.158^{+0.018}_{-0.023}$			
	$\chi^2/\text{d.o.f}$				$3673.1/3383$			

Note. Best-fit parameters for the model **tbabs\*(diskbb+relxill+cutoffpl)**. Parameters with \* are fixed during the fit and the symbol  $P$  denotes the upper or lower boundary. Parameters that are only shown for Epoch 4 are tied across all observations.

TABLE 4  
BEST-FIT VALUES WITH RELXILLD.

Component	Parameter	Epoch 1	Epoch 2	Epoch 3	Epoch 4	Epoch 5	Epoch 6	Epoch 7
TBABS	$N_{\text{H}}$ ( $10^{22}$ cm $^{-2}$ )				$0.98^{+0.04}_{-0.04}$			
DISKBB	$T_{\text{in}}$ (keV)	$0.48^{+0.04}_{-0.04}$	$0.561^{+0.012}_{-0.014}$	$0.659^{+0.008}_{-0.008}$	$0.717^{+0.008}_{-0.01}$	$0.726^{+0.006}_{-0.007}$	$0.762^{+0.008}_{-0.007}$	$0.756^{+0.008}_{-0.006}$
RELXILL	$a_*$				$> 0.87$			
	$q_{\text{in}}$	3*	3*	3*	$7.9^{+P}_{-4}$	$7.3^{+P}_{-2.2}$	$7.2^{+P}_{-2.7}$	$6.5^{+P}_{-1.4}$
	$q_{\text{out}}$				3*			
	$R_{\text{br}}$ ( $R_{\text{g}}$ )	-	-	-	$3.7^{+0.7}_{-0.4}$	$3.8^{+1.0}_{-0.6}$	$3.8^{+1.2}_{-0.6}$	$4.2^{+1.1}_{-0.8}$
	Incl				$35.3^{+1.5}_{-1.5}$			
	$A_{\text{Fe}}$				$> 8.6$			
	$R_{\text{in}}$ (ISCO)	$11^{+P}_{-6}$	$1.5^{+0.8}_{-P}$	$1.5^{+0.9}_{-P}$	$1.69^{+0.22}_{-0.23}$	$1.7^{+0.3}_{-0.4}$	$1.77^{+0.29}_{-0.26}$	$1.73^{+0.25}_{-0.18}$
	$\log(\xi)$	$3.97^{+0.17}_{-0.19}$	$3.69^{+0.17}_{-0.14}$	$4.2^{+0.1}_{-0.1}$	$3.49^{+0.13}_{-0.15}$	$4.00^{+0.22}_{-0.16}$	$4.0^{+0.2}_{-0.4}$	$4.01^{+0.27}_{-0.4}$
	$\log(n_e)$	$16^{+P}_{-P}$	$19.0^{+P}_{-0.6}$	$19.0^{+P}_{-0.6}$	$18.9^{+P}_{-0.9}$	$17.9^{+0.4}_{-1.3}$	$18.2^{+0.5}_{-0.5}$	$15.0^{+2.1}_{-P}$
CUTOFFPL	$\Gamma$	$1.724^{+0.026}_{-0.019}$	$2.042^{+0.024}_{-0.011}$	$2.166^{+0.04}_{-0.022}$	$2.369^{+0.019}_{-0.029}$	$2.387^{+0.023}_{-0.024}$	$2.43^{+0.04}_{-0.04}$	$2.54^{+0.09}_{-0.06}$
	$E_{\text{cut}}$ (keV)	$100^{+18}_{-14}$	$130^{+30}_{-20}$	$> 270$	$> 320$	$> 310$	$> 390$	$170^{+270}_{-90}$
<b>cflux</b>								
$F_{\text{diskbb}}$	( $10^{-8}$ erg cm $^{-2}$ s $^{-1}$ )	$0.22^{+0.04}_{-0.03}$	$0.556^{+0.027}_{-0.029}$	$0.965^{+0.017}_{-0.017}$	$1.346^{+0.028}_{-0.012}$	$1.390^{+0.027}_{-0.017}$	$1.634^{+0.029}_{-0.012}$	$1.82^{+0.05}_{-0.03}$
$F_{\text{relxillD}}$	( $10^{-8}$ erg cm $^{-2}$ s $^{-1}$ )	$0.55^{+0.09}_{-0.08}$	$0.69^{+0.04}_{-0.1}$	$1.2^{+0.1}_{-0.1}$	$1.43^{+0.11}_{-0.3}$	$1.28^{+0.13}_{-0.11}$	$1.44^{+0.3}_{-0.18}$	$1.73^{+0.21}_{-0.22}$
$F_{\text{cutoffpl}}$	( $10^{-8}$ erg cm $^{-2}$ s $^{-1}$ )	$1.00^{+0.09}_{-0.05}$	$1.21^{+0.11}_{-0.06}$	$0.75^{+0.07}_{-0.19}$	$1.54^{+0.1}_{-0.14}$	$1.53^{+0.08}_{-0.11}$	$1.51^{+0.11}_{-0.3}$	$1.6^{+0.6}_{-0.6}$
constant	ME/LE				$1.025^{+0.016}_{-0.014}$			
	HE/LE				$1.088^{+0.022}_{-0.021}$			
	$\chi^2/\text{d.o.f}$				3664.5/3376			

Note. Best-fit parameters for the model `tbabs*(diskbb+relxillD+cutoffpl)`. Parameters with \* are fixed during the fit and the symbol  $P$  denotes the upper or lower boundary. Parameters that are only shown for Epoch 4 are tied across all observations.

TABLE 5  
BEST-FIT VALUES WITH RELXILLCP (MODEL 2).

Component	Parameter	Epoch 1	Epoch 2	Epoch 3	Epoch 4	Epoch 5	Epoch 6	Epoch 7
<b>tbabs</b>	$N_{\text{H}}$ ( $10^{22}$ cm $^{-2}$ )				$0.73^{+0.06}_{-0.06}$			
<b>diskbb</b>	$T_{\text{in}}$ (keV)	$0.48^{+0.04}_{-0.04}$	$0.567^{+0.016}_{-0.016}$	$0.676^{+0.009}_{-0.01}$	$0.729^{+0.008}_{-0.009}$	$0.739^{+0.008}_{-0.009}$	$0.775^{+0.008}_{-0.009}$	$0.768^{+0.008}_{-0.009}$
<b>relxillcp</b>	$a_*$				$> 0.85$			
	$q_{\text{in}}$	3*	3*	3*	$10^{+P}_{-3}$	$8.0^{+P}_{-2.2}$	$9^{+P}_{-4}$	$7.3^{+P}_{-2.0}$
	$q_{\text{out}}$				3*			
	$R_{\text{br}}$ ( $R_{\text{g}}$ )	-	-	-	$3.42^{+0.6}_{-0.12}$	$3.9^{+0.9}_{-0.7}$	$3.6^{+2.1}_{-0.3}$	$4.1^{+1.2}_{-0.9}$
	Incl				$37.1^{+1.4}_{-1.3}$			
	$A_{\text{Fe}}$				$10.0^{+P}_{-0.3}$			
	$R_{\text{in}}$ (ISCO)	$> 12$	$2.3^{+1.8}_{-0.8}$	$2.5^{+1.8}_{-1.1}$	$1.1^{+0.7}_{-P}$	$1.1^{+0.4}_{-P}$	$1.18^{+0.5}_{-0.12}$	$1.1^{+0.6}_{-P}$
	$\log(\xi)$	$4.56^{+0.05}_{-0.11}$	$4.46^{+0.13}_{-0.1}$	$4.66^{+P}_{-0.07}$	$3.99^{+0.12}_{-0.15}$	$4.09^{+0.24}_{-0.18}$	$4.27^{+0.12}_{-0.24}$	$3.93^{+0.22}_{-0.3}$
<b>nthcomp</b>	$\Gamma$	$1.773^{+0.04}_{-0.024}$	$2.092^{+0.019}_{-0.022}$	$2.215^{+0.03}_{-0.027}$	$2.339^{+0.02}_{-0.016}$	$2.360^{+0.022}_{-0.023}$	$2.391^{+0.024}_{-0.018}$	$2.42^{+0.12}_{-0.08}$
	$kT_{\text{e}}$ (keV)	$64^{+30}_{-21}$	$160^{+600}_{-70}$	$> 270$	$> 400$	$> 310$	$> 410$	$65^{+600}_{-30}$
<b>cflux</b>								
$F_{\text{diskbb}}$	( $10^{-8}$ erg cm $^{-2}$ s $^{-1}$ )	$0.183^{+0.03}_{-0.024}$	$0.506^{+0.024}_{-0.022}$	$0.938^{+0.025}_{-0.012}$	$1.370^{+0.022}_{-0.022}$	$1.421^{+0.024}_{-0.022}$	$1.665^{+0.023}_{-0.022}$	$1.86^{+0.03}_{-0.03}$
$F_{\text{relxillcp}}$	( $10^{-8}$ erg cm $^{-2}$ s $^{-1}$ )	$0.94^{+0.15}_{-0.25}$	$0.85^{+0.12}_{-0.15}$	$1.10^{+0.12}_{-0.14}$	$1.04^{+0.09}_{-0.07}$	$1.05^{+0.09}_{-0.07}$	$1.09^{+0.11}_{-0.09}$	$1.11^{+0.6}_{-0.19}$
$F_{\text{nthcomp}}$	( $10^{-8}$ erg cm $^{-2}$ s $^{-1}$ )	$0.50^{+0.24}_{-0.15}$	$0.67^{+0.11}_{-0.08}$	$0.46^{+0.08}_{-0.08}$	$0.528^{+0.022}_{-0.027}$	$0.50^{+0.03}_{-0.03}$	$0.43^{+0.03}_{-0.03}$	$0.34^{+0.04}_{-0.06}$
	$L_{0.1-100\text{keV}}/L_{\text{Edd}}$ (%)	10.4	12.9	15.9	18.8	19.0	20.3	21.1
<b>constant</b>	ME/LE				$1.022^{+0.014}_{-0.012}$			
	HE/LE				$1.147^{+0.034}_{-0.025}$			
	$\chi^2/\text{d.o.f}$				3737.3/3383			

Note. Best-fit parameters for the model **tbabs\*(diskbb+relxillcp+cutoffpl)**. Parameters with \* are fixed during the fit and the symbol  $P$  denotes the upper or lower boundary. Parameters that are only shown for Epoch 4 are tied across all observations.

TABLE 6  
BEST-FIT VALUES WITH SIMPLCUT (MODEL 3).

Component	Parameter	Epoch 1	Epoch 2	Epoch 3	Epoch 4	Epoch 5	Epoch 6	Epoch 7
<b>tbabs</b>	$N_{\text{H}}$ ( $10^{22}$ cm $^{-2}$ )				$0.75^{+0.04}_{-0.06}$			
<b>diskbb</b>	$T_{\text{in}}$ (keV)	$0.50^{+0.04}_{-0.04}$	$0.575^{+0.018}_{-0.017}$	$0.682^{+0.008}_{-0.009}$	$0.735^{+0.007}_{-0.007}$	$0.743^{+0.007}_{-0.01}$	$0.777^{+0.007}_{-0.007}$	$0.769^{+0.008}_{-0.009}$
<b>relxillcp</b>	$a_*$				$0.92^{+0.05}_{-0.07}$			
	$q_{\text{in}}$	3*	3*	3*	$9.7^{+P}_{-3}$	$7.8^{+P}_{-2.3}$	$8.9^{+P}_{-5}$	$7.0^{+P}_{-2.0}$
	$q_{\text{out}}$				3*			
	$R_{\text{br}}$ ( $R_{\text{g}}$ )	-	-	-	$3.32^{+0.5}_{-0.15}$	$3.8^{+1}_{-0.4}$	$3.45^{+2.6}_{-0.28}$	$4.0^{+1.5}_{-0.7}$
	Incl				$37.3^{+1.4}_{-1.1}$			
	$A_{\text{Fe}}$				$10.0^{+P}_{-0.3}$			
	$R_{\text{in}}$ (ISCO)	$50.0^{+P}_{-39}$	$3.0^{+1.9}_{-0.9}$	$3.1^{+1.0}_{-0.9}$	$1.4^{+0.5}_{-P}$	$1.41^{+0.25}_{-0.30}$	$1.47^{+0.24}_{-0.29}$	$1.4^{+0.5}_{-0.3}$
	$\log(\xi)$	$4.62^{+0.03}_{-0.04}$	$4.59^{+0.09}_{-0.15}$	$4.70^{+P}_{-0.19}$	$3.99^{+0.12}_{-0.16}$	$4.13^{+0.22}_{-0.22}$	$4.28^{+0.13}_{-0.24}$	$3.94^{+0.6}_{-0.27}$
	$\Gamma$	$1.771^{+0.008}_{-0.012}$	$2.125^{+0.024}_{-0.022}$	$2.243^{+0.04}_{-0.029}$	$2.356^{+0.03}_{-0.018}$	$2.370^{+0.019}_{-0.022}$	$2.397^{+0.019}_{-0.016}$	$2.43^{+0.11}_{-0.07}$
	$kT_{\text{e}}$ (keV)	$90^{+35}_{-20}$	> 80	> 240	> 280	> 200	> 270	$60^{+230}_{-30}$
<b>simplcut</b>	$f_{\text{sc}}$	$0.121^{+0.004}_{-0.011}$	$0.175^{+0.06}_{-0.028}$	$0.127^{+0.04}_{-0.023}$	$0.119^{+0.007}_{-0.006}$	$0.114^{+0.01}_{-0.012}$	$0.0947^{+0.0025}_{-0.008}$	$0.076^{+0.01}_{-0.015}$
<b>cflux</b>								
$F_{\text{diskbb}}$	( $10^{-8}$ erg cm $^{-2}$ s $^{-1}$ )	$0.215^{+0.03}_{-0.028}$	$0.60^{+0.06}_{-0.03}$	$1.066^{+0.06}_{-0.024}$	$1.547^{+0.022}_{-0.029}$	$1.60^{+0.05}_{-0.04}$	$1.838^{+0.021}_{-0.029}$	$2.009^{+0.025}_{-0.04}$
$F_{\text{relxillcp}}$	( $10^{-8}$ erg cm $^{-2}$ s $^{-1}$ )	$1.278^{+0.017}_{-0.014}$	$1.17^{+0.1}_{-0.11}$	$1.34^{+0.05}_{-0.21}$	$1.21^{+0.11}_{-0.09}$	$1.18^{+0.09}_{-0.09}$	$1.20^{+0.08}_{-0.09}$	$1.2^{+0.7}_{-0.4}$
	$L_{0.1-100\text{keV}}/L_{\text{Edd}}$ (%)	10.5	13.7	16.8	19.7	19.7	21.0	21.7
<b>constant</b>	ME/LE				$1.018^{+0.017}_{-0.007}$			
	HE/LE				$1.141^{+0.020}_{-0.027}$			
	$\chi^2/\text{d.o.f}$				3734.8/3383			

*Note.* Best-fit parameters for the model **tbabs\*simplcut(diskbb+relxillcp)** with a broken power-law emissivity. Parameters with \* are fixed during the fit and the symbol  $P$  denotes the upper or lower boundary. Parameters that are only shown for Epoch 4 are tied across all observations. The model flux is before Comptonization by **simplcut**. The absorption corrected X-ray flux is calculated with the **flux** command in **XSPEC**.



TABLE 7  
BEST-FIT VALUES WITH REFHIDDEN (MODEL 4).

Component	Parameter	Epoch 1	Epoch 2	Epoch 3	Epoch 4	Epoch 5	Epoch 6	Epoch 7
<b>tbabs</b>	$N_{\text{H}}$ ( $10^{22}$ cm $^{-2}$ )				$0.36^{+0.09}_{-0.06}$			
<b>relconv</b>	$a_*$				0.998*			
	$q_{\text{in}}$	$2.0^{+2.0}_{-2.2}$	$2.17^{+0.21}_{-0.16}$	$1.7^{+0.5}_{-0.6}$	$2.35^{+0.14}_{-0.14}$	$3.3^{+0.7}_{-0.6}$	$2.7^{+0.5}_{-0.3}$	$2.5^{+0.8}_{-0.3}$
	$q_{\text{out}}$				= $q_{\text{in}}$			
	Incl				$33.2^{+2.4}_{-1.4}$			
	$R_{\text{in}}$ (ISCO)	$9^{+P}_{-P}$	$1.5^{+5}_{-P}$	$1.0^{+20}_{-P}$	$1.6^{+2.8}_{-P}$	$5.1^{+2.5}_{-1.7}$	$3.8^{+4}_{-1.8}$	$2.6^{+2.9}_{-1.5}$
<b>refhidden</b>	$kT_{\text{bb}}$ (keV)	$0.487^{+0.013}_{-0.008}$	$0.400^{+0.007}_{-P}$	$0.400^{+0.005}_{-P}$	$0.441^{+0.004}_{-0.004}$	$0.4403^{+0.004}_{-0.0027}$	$0.459^{+0.004}_{-0.004}$	$0.468^{+0.005}_{-0.004}$
	$H_{\text{den}}$ ( $10^{20}$ cm $^{-3}$ )	> 86	$16.2^{+4.0}_{-1.8}$	$5.7^{+0.6}_{-0.7}$	$5.3^{+0.4}_{-0.5}$	$4.4^{+0.5}_{-0.3}$	$5.4^{+0.3}_{-0.4}$	$5.6^{+0.4}_{-0.4}$
	Illum/BB	$1.8^{+0.5}_{-0.4}$	$1.82^{+0.1}_{-0.29}$	$1.27^{+0.06}_{-0.2}$	$0.84^{+0.09}_{-0.11}$	$0.97^{+0.3}_{-0.04}$	$0.77^{+0.14}_{-0.07}$	$0.52^{+0.18}_{-0.06}$
	Norm	$0.39^{+0.03}_{-0.03}$	$0.70^{+0.06}_{-0.05}$	$0.89^{+0.04}_{-0.04}$	$0.86^{+0.15}_{-0.09}$	$0.99^{+0.19}_{-0.09}$	$0.92^{+0.07}_{-0.21}$	$0.73^{+0.2}_{-0.11}$
<b>simplcut</b>	$f_{\text{sc}}$	$0.773^{+0.011}_{-0.015}$	$0.417^{+0.015}_{-0.03}$	$0.293^{+0.009}_{-0.017}$	$0.163^{+0.005}_{-0.004}$	$0.132^{+0.006}_{-0.009}$	$0.132^{+0.003}_{-0.003}$	$0.110^{+0.013}_{-0.011}$
	$\Gamma$	$1.867^{+0.013}_{-0.009}$	$2.124^{+0.015}_{-0.018}$	$2.283^{+0.013}_{-0.025}$	$2.305^{+0.012}_{-0.016}$	$2.315^{+0.026}_{-0.013}$	$2.381^{+0.014}_{-0.021}$	$2.42^{+0.05}_{-0.06}$
	$kT_e$ (keV)	$26.4^{+1.6}_{-2.1}$	$50^{+10}_{-10}$	> 200	> 100	> 100	> 360	$70^{+500}_{-30}$
	$L_{0.1-100\text{keV}}/L_{\text{Edd}}$ (%)	8.2	9.3	11.0	12.2	12.5	13.3	12.8
<b>constant</b>	ME/LE				$0.985^{+0.008}_{-0.006}$			
	HE/LE				$1.057^{+0.016}_{-0.019}$			
	$\chi^2/\text{d.o.f}$				3788.8/3386			

*Note.* Best-fit parameters for the model **tbabs\*simplcut\*relconv\*refhidden** with a power-law emissivity. Parameters with \* are fixed during the fit and the symbol  $P$  denotes the upper or lower boundary. Parameters that are only shown for Epoch 4 are tied across all observations. The absorption corrected X-ray flux is calculated with the **flux** command in **XSPEC**.